Nanoscale

Accepted Manuscript

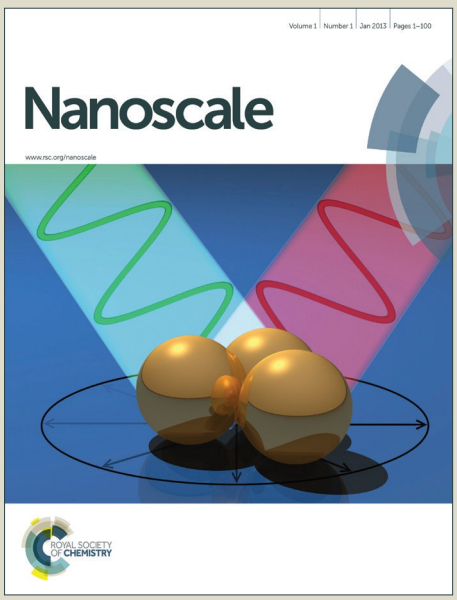

ROYAL SOCIETY OF CHEMISTRY

www.rsc.org/nanoscale

Cite this: DOI: 10.1039/c0xx00000x

www.rsc.org/xxxxxx

ARTICLE TYPE

NaV_3O_8 Nanosheets@Polypyrrole Core-Shell Composites with Good Electrochemical Performance as Cathode for Na-Ion Batteries

Hongyan Kang, Yongchang Liu, Minghui Shang, Tianyu Lu, Yijing Wang and Lifang Jiao*

Received (in XXX, XXX) Xth XXXXXXXXX 20XX, Accepted Xth XXXXXXXXX 20XX

DOI: 10.1039/b000000x

Novel NaV_3O_8 nanosheets@polypyrrole core-shell composites have been successfully prepared for the first time *via* a chemical oxidative polymerization method. Based on the morphological and microstructural characterization, it was found that the polypyrrole (PPy) was uniformly wrapped on the surfaces of the NaV_3O_8 nanosheets. When used as cathode for Na-ion batteries, the as-synthesized NaV_3O_8@10% PPy composite shows significantly improved cycling performance (with a discharge capacity of 99 mAh g^{-1} after 60 cycles at 80 mA g^{-1}) and better rate capacity (with a discharge capacity of 63 mAh g^{-1} at a high current density of 640 mA g^{-1}) than pristine NaV_3O_8 nanosheets. The greatly enhanced performance benefits from the unique core-shell structure, where the PPy coating not only prevents the pulverization and aggregation of the lamellar NaV_3O_8 nanosheets during cycling, which can improve the cycling stability, but also enhances the electrical conductivity of the composite, which can facilitate Na^+ ion diffusion.

Introduction

With the rapid development of society, the need for building a large-scale energy storage system (ESS) has been more and more urgent. The application of lithium-ion batteries (LIBs) is limited in this area, however, on account of the high cost and scarce natural resources of lithium.[1-3] Thus, it is very necessary to seek alternative materials for sustainable energy storage. Na-ion batteries (NIBs) with the advantages of low cost and natural abundance have been regarded as one of the possible alternatives to LIBs.[4-7] Due to the higher redox potential of Na/Na^+, however, and the larger ionic radius of Na^+, many materials used for NIBs have ended up showing low capacity, inferior rate performance and poor cycling stability.[8] Therefore, the task of finding suitable materials to store Na^+ has become a top priority of the sodium-ion battery industry.

In recent years, phosphorus-based polyanion materials, such as $NaFePO_4$,[9] $Na_2MnP_2O_7$,[10] $Na_2CoP_2O_7$,[11], $Na_{1.5}VPO_{4.8}F_{0.7}$,[12] $Na_3V_2(PO_4)_3$/C,[13,14] and $Na_7V_4(P_2O_7)_4(PO_4)$/C,[15] have been studied as cathode for NIBs and present good electrochemical performance. For example, Barpanda *et al*. studied the electrochemistry properties of layered $Na_2CoP_2O_7$, which delivered a discharge capacity of 80 mA h g^{-1} at a rate of 0.05 C.[11] Zhu *et al.* successfully synthesized carbon-coated $Na_3V_2(PO_4)_3$ embedded in porous carbon matrix, which can be (dis)charged in 6 s with a current density as high as 22A g^{-1}, still delivering a specific capacity of 44 mA h g^{-1}.[13] Their specific capacities still are not high enough to meet the requirements of the applications, however.

Currently, vanadium oxides and their derivative compounds have been gaining more and more attention because of their high capacity and low cost.[16-21] They can form many-layered and nanoscale compounds with open structural frameworks, making them prospective materials for ion intercalation, exchange, and storage.[22] For example, Su *et al*. prepared single-crystalline bilayered V_2O_5 nanobelts to serve as cathode for NIBs, and they present a high capacity of 231.4 mA h g^{-1} and retained 170 mA h g^{-1} after 100 cycles at 80 mA g^{-1}.[23] NaV_6O_{15} nanorods synthesized by a facile hydrothermal method showed an initial discharge capacity of 142 mA h g^{-1}.[24] As a member of the vanadium oxide family, NaV_3O_8 has also been proved to be a promising material for Na-ion storage.[25,26] It consists of $V_3O_8^-$ layers oriented along the *a* axis, jointed by sodium ions at the octahedral sites in the interlayer. The sodium ions act as "pins" to prevent the collapse of $V_3O_8^-$ layers during charge and discharge processes.[27] Nevertheless, just like other vanadates, the poor electrical conductivity and unstable structure of NaV_3O_8 lead to capacity fading and poor rate performance upon prolonged cycling.

As is well known, coating conducting polymer is an effective way to improve the electrical performance of active materials.[28-31] With the features of excellent electrical conductivity, environmental stability and easy synthesis, polypyrrole (PPy) has been one of the most attractive conductive polymers.[32-34] Various materials have been prepared with PPy coatings, which demonstrate excellent cycling stability and high-rate capability, such as RGO/PPy,[35] MoO_3/PPy,[36] and S/PPy.[37] The highly improved electrochemical performance of the active materials is owing to the excellent properties of PPy: On one hand, PPy can serve as a conductive agent to reduce migration resistance of ions, on the other hand, PPy acts as a protective layer, shielding the active material's structure from pulverization and

aggregation. Nevertheless, to the best of our knowledge, there has been few report on NaV_3O_8@PPy composite as cathode for Na-ion batteries.

In view of the above analysis, NaV_3O_8@PPy composites have been fabricated as cathode material for Na-ion batteries, with the aim of improving the cycling stability and high-rate capacity. In this paper, we have successfully prepared novel core-shell nanostructured NaV_3O_8@PPy composites for the first time, and used them as cathode materials for NIBs. Scanning and transmission electron microscopy (SEM and TEM) results demonstrated that the PPy was evenly coated on the surfaces of the NaV_3O_8 nanosheets. Compared with bare NaV_3O_8 nanosheets, NaV_3O_8@10% PPy composite delivered greatly improved cycling stability, with a high capacity of 99 mA h g^{-1} after 60 cycles at 80 mA g^{-1} .

Experimental section

Materials synthesis

All chemical reagents used in this experiment were of analytical grade. Pyrrole monomer was distilled before use.

NaV_3O_8 nanosheets were prepared *via* a facile sol−gel route with subsequent calcination in air. In a typical synthesis, stoichiometric amounts of V_2O_5 (1.2 g) and oxalic acid with a molar ratio of 1:3 were added into a beaker containing 40 mL of deionized water. The suspension was kept at 70 ℃ under magnetic stirring until a clear blue solution formed. The reaction can be expressed as follows:

$$V_2O_5 + 3H_2C_2O_4 \rightarrow 2VOC_2O_4 + 2CO_2\uparrow + 3H_20 \quad (1)$$

Then, a stoichiometric amount of $NaNO_3$ (Na:V=1:3) was added into the obtained blue solution. After stirring for 1 h, the mixture solution was dried at 80 ℃ to evaporate water. Then, the dry gel was calcined at 400 ℃ in air for 8 h.

The core-shell nanostructured NaV_3O_8@PPy composites were prepared *via* a chemical oxidative polymerization method. First, 0.1 g NaV_3O_8 was uniformly dispersed in deionized water. Then 11.3 μL pyrrole (Py) monomer (mass ratio of NaV_3O_8: Py = 90:10) was slowly injected into the suspension. After stirring for 0.5 h, sodium p-toluenesulfonate as doping agent and $FeCl_3$ as oxidation agent were dissolved into the above solution. The mixture was kept at 0-5 ℃ for 6 h to complete the polymerization reaction. The obtained composite was designated as NaV3O8@10% PPy. NaV3O8@PPy composite with the adding of 25.7 μL pyrrole monomer (mass ratio of NaV3O8: Py = 80:20) was also prepared and designated as NaV_3O_8@20% PPy. Pure PPy was synthesized by the same method without adding NaV_3O_8 The schematic illustration of the process for synthesizing the core-shell nanostructured NaV_3O_8@PPy composites is shown in Scheme 1.

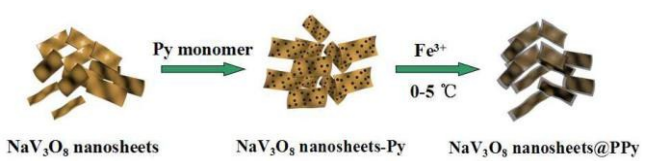

Scheme 1 Schematic illustration of the synthesis of core-shell nanostructured NaV_3O_8@PPy composites.

Characterization

The exact amounts of PPy in NaV_3O_8@PPy composites were determined by Thermogravimetric analysis (TG, SETARAM S60). The structure of the materials was characterized by X-ray diffraction (XRD, Rigaku D/Max-2500, Cu Kα radiation, λ=1.5408 Å) in the 2θ range of 3-80° at a scan rate of 4° min^{-1}. Fourier transform infrared (FT-IR) spectra were recorded on a FT-TR-650 spectrometer (Tianjin Gangdong).The morphology and microstructure were observed by scanning electron microscope (SEM, HITACHI S-4800) and transmission electron microscope (TEM, Tecnai G2 F20). X-ray photoelectron spectroscopy (XPS) was carried out on the PHI5000 VersaProbe.

Electrochemical measurements

The cathodes were prepared by adding the active material, polyvinylidene fluoride (PVDF) and Super P Li in the weight ratio of 70:10:20 to N-methyl pyrrolidone (NMP) solvent to form homogeneous slurry. The slurry was cast onto a Al foam and dried at 80℃ for 12 h in vacuum. The cells were assembled in an argon filled glove box. The counter electrode was metallic sodium foil and the electrolyte was 1M $NaPF_6$ dissolved in a mixture of ethylene carbonate and dimethyl carbonate (EC/DMC=1/1 by volume). Galvanostatic charge-discharge tests were carried out in the potential window of 1.5-4.0 V on a Land battery tester (CT2001A). Cyclic voltammetry (at a scan rate of 0.1 mV s^{-1}) and electrochemical impedance spectrocopy (frequency range: 0.1-10^5 Hz) were performed on a CHI 660b electrochemical workstation (Chenhua, Shanghai, China).

Results and discussion

Fig. 1a shows the XRD patterns of the as prepared NaV_3O_8 and NaV_3O_8@PPy composites. The main diffraction peaks have been marked. All of the materials exhibit similar XRD patterns, which can be readily indexed to monoclinic crystalline $Na_{1.1}V_3O_{7.9}$ phase (space group *P21/m*, JCPDS card 45-0498), except several weak impurity peaks (marked by ★, NaV_6O_{15}, JCPDS 24-1155) The results are consistent with previous reports.[38, 39] There are no peaks for PPy, indicating that the PPy is present in amorphous form.

Fig. 1b shows the FT-IR spectra of the as prepared NaV_3O_8, NaV_3O_8@10% PPy composite and pure PPy. For bare NaV_3O_8, the peaks located at 996 cm^{-1} and 954 cm^{-1} are corresponding to V=O vibrations, while those at 759 cm^{-1} and 564 cm^{-1} are attributed to asymmetric and symmetric stretching vibrations of V-O-V.[25] In addition, the peak at 1400 cm^{-1} is due to Na-O vibrations,[40] and the absorption band at 1634 cm^{-1} reflects the O-H vibrations of water. As for pure PPy, the characteristic peaks of PPy are located at 1532 $cm^{-1}$and 1444 cm^{-1}, which are ascribed to the antisymmetric and symmetric ring-stretching modes, respectively.[41] Peaks situated at 1147 cm^{-1} and 863 cm^{-1} indicate the doping state of PPy.[42] Furthermore, peaks at 1030 cm^{-1} and 1288 cm^{-1} reflect the C-H deformation vibrations and C-N stretching vibrations, respectively.[42] For NaV_3O_8@10% PPy composite, it presents all the characteristic peaks of NaV_3O_8 and PPy, confirming the presence of both NaV_3O_8 and PPy.

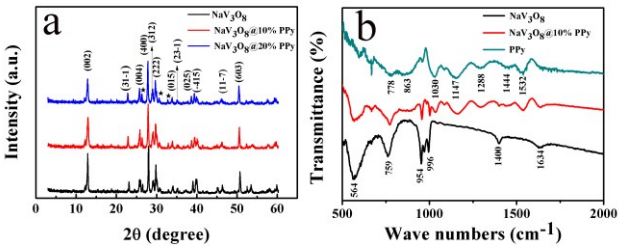

Fig. 1 (a) XRD patterns of the as-prepared bare NaV_3O_8 and NaV_3O_8@PPy composites. (b) FT-IR spectra of NaV_3O_8, NaV_3O_8@10% PPy and pure PPy.

The accurate amounts of PPy in the NaV_3O_8@PPy composites were estimated by thermogravimetric analysis (TGA) and the results are shown in Fig. 2. The samples were heated at the rate of 5℃ min^{-1} in an air atmosphere. For NaV_3O_8, there is no weight loss over such a temperature except for the remove of moisture in NaV_3O_8. And for other samples, the first weight loss from room temperature to around 200 ℃ was attributed to the loss of physical adsorbed water and the subsequent degradation around 270 °C can be ascribed to the decomposition of PPy. Based on the TG analysis, the weight contents of PPy in NaV_3O_8@10% PPy and NaV_3O_8@20% PPy were approximately calculated to be 8.2 % and 19.8 %, respectively.

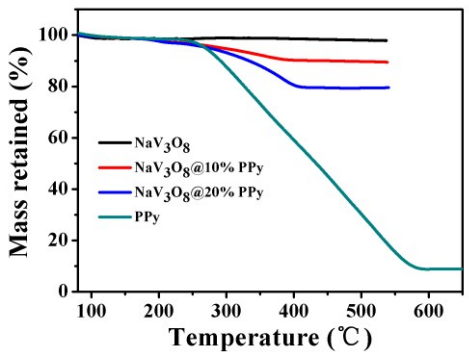

Fig. 2 TG curves of bare NaV_3O_8, NaV_3O_8@PPy composites and PPy.

Fig. 3 displays SEM images of NaV_3O_8@PPy composites and pure PPy. As shown in Fig. 3a, The NaV_3O_8 nanosheets have been synthesized with a thickness around 50 nm and a length of 300-500 nm. Compared with the bare NaV_3O_8, the surfaces of NaV_3O_8@10% PPy (Fig. 3b) and NaV_3O_8@20% PPy (Fig. 3c) have become rough and we can clearly see that there is a layer of PPy coated on the surfaces of NaV_3O_8 nanosheets. Fig. 3d shows the SEM image of the pure PPy, which are particles with sizes of about 1 μm, most of which are aggregated. It is obvious that the pure PPy particles are much larger than those coated on the surfaces of the NaV_3O_8 nanosheets. Thus, we speculate that pyrrole monomers are firstly adsorbed on the surfaces of NaV_3O_8 nanosheets by electrostatic forces, and then the polymerization reaction occurs directly on the NaV_3O_8 nanosheets surfaces. During the polymerization, the presence of the NaV_3O_8 nanosheets not only can suppress the growth of PPy particles, but also can prevent the PPy particles from aggregating. Thus, the tiny PPy particles can uniformly coat on the surfaces of the NaV_3O_8 nanosheets.

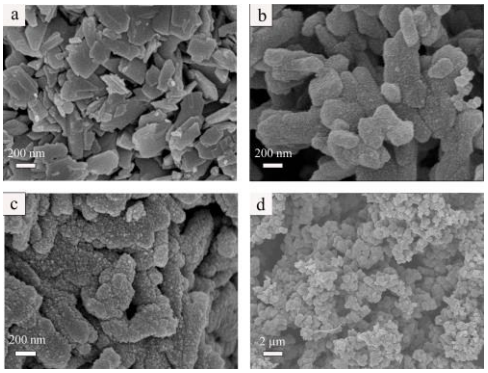

Fig. 3 SEM images of (a) the as-prepared bare NaV_3O_8, (b) NaV_3O_8@10% PPy, (c) NaV_3O_8@20% PPy and (d) pure PPy.

Fig. 4 shows TEM images of the NaV_3O_8@PPy composites and a high resolution TEM (HR-TEM) image of NaV_3O_8@10% PPy. Fig. 4a indicates that the bare NaV_3O_8 nanosheet has a smooth surface. Fig. 4b and 4c further demonstrate that the novel core-shell nanostructured NaV_3O_8@PPy composites have been successfully synthesized. As displayed in Fig. 4b, the PPy coating is about 25-30 nm in thickness, and there is no extra PPy, indicating that the amount of PPy is suitable. As for NaV_3O_8@20% PPy (Fig. 4c), the thickness of the PPy is about 90 nm, and there is some isolated PPy scattered around the composite, indicating that the amount of PPy is excessive. Too much PPy will decrease the content of active materials and increase Na^+ transportation time, resulting in lower discharge capacity. As shown in the HR-TEM image of NaV_3O_8@10% PPy (Fig. 4d), an amorphous PPy layer is coated on the surface of a NaV_3O_8 nanosheet. Moreover, there are clear lattice fringes with an interplanar spacing of 0.69 nm, corresponding well to the (002) planes of monoclinic NaV_3O_8.

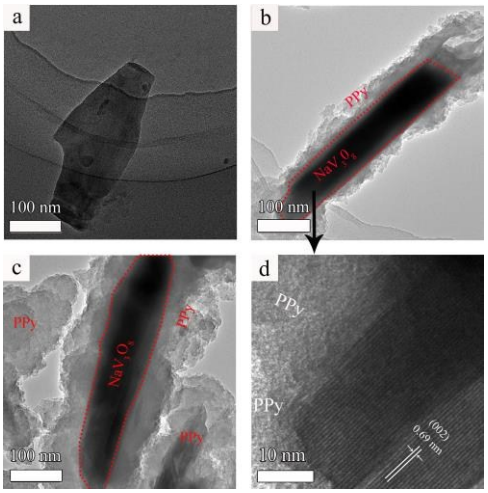

Fig. 4 TEM images of (a) the as-prepared bare NaV_3O_8, (b) NaV_3O_8@10% PPy, (c) NaV_3O_8@20% PPy and (d) HR-TEM image of NaV_3O_8@10% PPy.

Fig.5a shows the first three continuous cyclic voltammetry (CV) curves of NaV_3O_8@10% PPy electrode at a scan rate of 0.1 mV s^{-1} over the voltage range of 1.5-4.0 V. There are two distinct pairs of redox peaks located at 3.35 and 2.35 V (cathodic), and at 3.47 and 2.61 V (anodic), and all the redox peaks are almost overlapping in the first three cycles. The two pairs of redox peaks

separation are 0.12 and 0.26 V, respectively, which are much smaller than the result in a previous report.[25] Both the highly overlapping redox peaks and the small separation in the spike potential suggest the good reversibility of sodium ions insertion/extraction. Fig. S1a shows the CV curves of bare NaV_3O_8, with two pairs of redox peaks similar to NaV_3O_8@10% composite. However, CV curves decline rapidly during the first three cycles. Fig. S2 gives the CV curves of pure PPy, which does not exhibit distinct peaks comparing to NaV_3O_8@10% composite. The mechanism of NaV_3O_8 will be discussed in the following XPS section.

Fig. 5b gives the charge/discharge profiles of NaV_3O_8@10% PPy at different cycles at a current density of 80 mA g^{-1}. There are two pairs of superimposable plateaus, with the discharge plateaus located at around 3.3 and 2.4 V, and the corresponding charge plateaus located at around 3.4 and 2.5 V, which is in good agreement with the CV results (shown in Figure 5a). The charge/discharge profiles at different cycles are overlap reasonably well, indicating the good structural reversibility of NaV_3O_8@10% PPy upon long cycling. Fig. S1b shows charge/discharge profiles of bare NaV_3O_8, with two pairs of plateaus similar to NaV_3O_8@10% PPy. However, the capacity of bare NaV_3O_8 electrode decreases quickly, implying the inferior cycle stability.

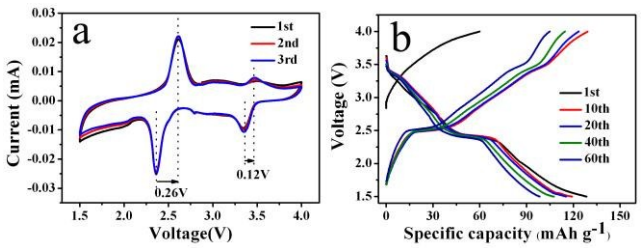

Fig. 5 (a) CV curves of the NaV_3O_8@10% PPy electrode for the first 3 cycles at a scan rate of 0.1 mV s^{-1}. (b) Charge/discharge profiles of the selected cycles for NaV_3O_8@10% PPy at 80 mA g^{-1}.

XPS spectra of NaV_3O_8@10% PPy composite at different stages were examined to explore the change in the chemical state of vanadium during Na-ion insertion/extraction process (Fig. 6). For all stages, the V 2p core-level spectra consist of V $2p_{1/2}$ and V $2p_{3/2}$ levels due to the spin−orbit splitting, separated by 7−8 eV.[43] Furthermore, V $2p_{3/2}$ was studied to deduce the oxidation states of vanadium. As shown in Fig. 6, the V $2p_{3/2}$ levels were all composed of V^{5+} and V^{4+} states, located at 517.3 and 516.0 eV. respectively, in agreement with reports in the literature.[44] In Fig. 6a, the fitted areas of the V^{5+} and V^{4+} components of the V $2p_{3/2}$ suggest that the V^{5+}:V^{4+} ratio is 0.96:0.04. The excess amount of V^{4+} probably results from the impurity NaV_6O_{15}.[45] When the cell was discharged to the first plateau, the V^{5+}:V^{4+} ratio decreased to 0.79:0.21 (Fig. 6b). Therefore, the first plateau (at 3.3 V) corresponding to the cathodic peak at 3.35V in the CV curves, is presumably due to partial reduction of V^{5+} to V^{4+}. Subsequently, when the cell was discharged down to the second plateau, the V^{5+}:V^{4+} ratio further decreased to 0.68:0.32 (Fig. 6c). Thus, the second plateau (at 2.4 V), in accordance with the cathodic peak (at 2.35 V) in the CV, could correspond to the further reduction of V^{5+} to V^{4+}. The studies add to a growing body of evidence to support the simple single-phase reaction mechanism of NaV_3O_8 put forward in previous report.[25] Namely, Na-ions insert into empty sites to form $Na_{1+x}V_3O_8$ in the discharge process, while in the charge process, Na-ions extract from $Na_{1+x}V_3O_8$. (eqn (2) as follows) The different potentials of the redox peaks are attributed to the sodium insertion into sites with different energies for holding Na ions.[46] To the best of our knowledge, this is the first time that the change in the oxidation state of vanadium during cycling has been reported for NaV_3O_8. Furthermore, the mechanism of impurity NaV_6O_{15} is also a multi-steps Na ions insertion/extraction processes.

$$NaV_3O_8 + xNa^+ + xe^- \leftrightarrow Na_{1+x}V_3O_8 \qquad (2)$$

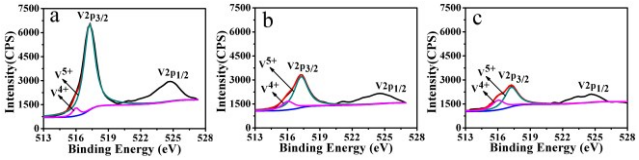

Fig. 6 XPS spectra of NaV_3O_8@10% PPy composite at different stages: V 2p peaks of (a) the cell in the charged state (b) the cell after discharge to 2.6 V (c) the cell after discharge to 2.2 V.

Fig. 7 gives the cycling performances of NaV_3O_8, NaV_3O_8@10% PPy, NaV_3O_8@20% PPy and PPy at the current density of 80 mA g^{-1} (0.23 C). The specific capacities of NaV_3O_8@PPy composites are calculated based on the total weight of active materials. The discharge capacity of PPy is very stable, and 30 mA h g^{-1} is retained after 60 cycles, which is much lower than that of NaV_3O_8. The bare NaV_3O_8 electrode delivers an initial discharge capacity of 140 mA h g^{-1}, however, the capacity fades fast and only 52 mA h g^{-1} is retained after 60 cycles, demonstrating the poor cycling stability. When the NaV_3O_8 was coated by PPy, the cycling performance was greatly improved. In particular, the NaV_3O_8@10% PPy electrode shows an initial capacity of 128.4 mA h g^{-1}, and it only shows any evidence of fading in the first few cycles, with a high capacity of 99 mA h g^{-1} retained over 60 cycles. The NaV_3O_8@20% PPy electrode delivers a lower capacity compared with NaV_3O_8@10% PPy, due to the low capacity of PPy. According to the above results, it can be assumed that PPy coating is a fairly effective way to improve the cycling stability of NaV_3O_8. The rate capabilities of the NaV_3O_8@10% PPy, NaV_3O_8 and PPy electrodes were further investigated, as shown in Fig.7b. The PPy electrode still shows a low capacity. The NaV_3O_8@10% PPy electrode presents excellent rate capability with high reversible discharge capabilities of 140, 119, 97, 79 and 63 mA h g^{-1} at the current densities of 0.23, 0.46, 0.92, 1.84 and 3.68 C (1 C=176 mA h g^{-1}), respectively. More importantly, when the current density is returned to 0.23 C, the capacity can recover to 130 mA h g^{-1}. By contrast, the rate capability of bare NaV_3O_8 is inferior with capacities of only 110, 91, 67, 47, and 30 mA h g^{-1} at the current densities of 0.23, 0.46, 0.92, 1.84 and 3.68 C. In short, NaV_3O_8@10% PPy exhibited higher reversible capacity, better cycling performance and rate capability than the bare NaV_3O_8. The achieved electrochemical performance of NaV_3O_8@10% PPy is also superior to those of previously reported NaV_3O_8 cathodes for NIBs.[25,26]

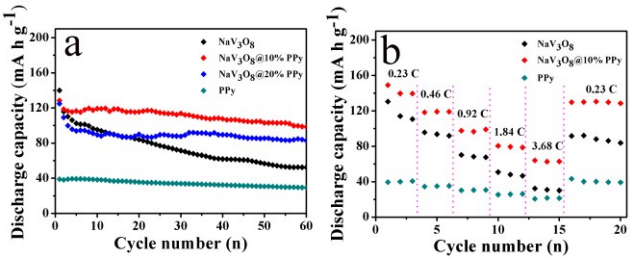

Fig. 7 Cycling performances (a) and rate performances (b) of NaV_3O_8, NaV_3O_8@ PPy composites and PPy.

In order to explore the reasons for the improved cycling stability of the NaV_3O_8@10% PPy composite, we compared the SEM image of the bare NaV_3O_8 electrode with that of the NaV_3O_8@10% PPy electrode after 60 charge/discharge cycles. Fig. 8a shows an image of the bare NaV_3O_8 electrode surface, where NaV_3O_8 nanosheets have aggregated into big compact bulks. We speculate that during the cycling, NaV_3O_8 nanosheets pulverize into pieces and the pieces aggregated into big bulks. The results powerfully illustrate why the capacity of the NaV_3O_8 fades so fast. As shown in Fig. 8b, the NaV_3O_8@10% PPy nanosheets structure can be retained on the whole, except for a few fragments. This excellent stability of the electrode can be attributed to the good coating of PPy on the surfaces of NaV_3O_8 nanosheets. PPy can buffer the volume change during charging/discharging to protect the NaV_3O_8 from splintering, resulting in highly improved cycling stability.

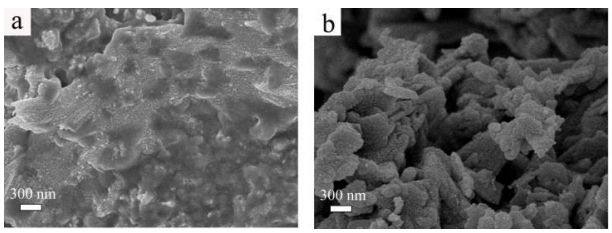

Fig. 8 SEM images of the electrodes after 60 cycles: (a) the as-prepared bare NaV_3O_8 and (b) the NaV_3O_8@10% PPy composite.

Fig. 9a shows electrochemical impedance spectra of the bare NaV_3O_8, NaV_3O_8@10% PPy, NaV_3O_8@20% PPy and pure PPy. All samples exhibit similar spectra with a compressed semicircle in the high-frequency region and an inclined line in the low-frequency region, implying that the electrochemical process is controlled by both charge transfer and Na-ions diffusion.[46] The semicircle diameter represents the charge-transfer resistance (Rct). Obviously, Pure PPy has the lowest Rct, followed by NaV_3O_8@10% PPy, NaV_3O_8@20% PPy and bare NaV_3O_8 exhibits the highest Rct. The decrease in Rct indicates that the PPy coating can reduce the resistance during cycling, which is ascribed to the conductive network of PPy, however, too much amount of PPy will increase the transfer time of electron. The result is in consistent with the best electrical performance of NaV_3O_8@10% PPy. And the line could be assigned to Warburg impedance, which is related to the diffusion of Na-ions into the bulk electrode material. The Na-ions diffusion coefficient can be calculated from the low frequency plots using the following equation[47]:

$$D = \frac{R^2T^2}{2A^2n^4F^4C^2\sigma^2} \quad (3)$$

Where R is the gas constant, T is the absolute temperature, A is the surface area, n is the number of electrons per molecule during oxidization, F is the Faraday constant, C is the concentration of Na-ions, and σ is the Warburg factor related to Z':

$$Z' = R_D + R_L + \sigma\omega^{-1/2} \quad (4)$$

Fig. 9b displays the relationship between Z' and $\omega^{-1/2}$ in the low frequency region. According to eqn (2) and eqn (3), it can be seen clearly that NaV_3O_8@10% PPy shows a largest Na-ions diffusion coefficient D_{Na+} among NaV_3O_8@20% PPy, NaV_3O_8@10% PPy and bare NaV_3O_8. Therefore, the proper PPy coating can extremely increase the electron conductivity and Na-ions diffusion, giving an improvement of electrochemical performance.

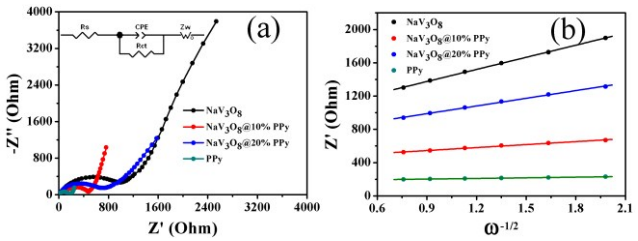

Fig. 9 (a) Nyquist impedance and equivalent circuit of the as-prepared bare NaV_3O_8, NaV_3O_8@10% PPy, NaV_3O_8@20% PPy and PPy. (b) The relationship between Z' and $\omega^{-1/2}$ in the low frequency region.

Conclusions

In summary, we have successfully prepared the core-shell nanostructured NaV_3O_8@polypyrrole composites *via* an *in-situ* chemical oxidative polymerization method and use them as cathodes for NIBs for the first time. The cycling stability and rate performance of the as-prepared NaV_3O_8@PPy composites have been substantially improved compared to bare NaV_3O_8. Among the tested samples, the NaV_3O_8@10% PPy electrode with a retained discharge capacity of 99 mA h g^{-1} after 60 cycles at 80 mA g^{-1} shows the best electrochemical performance. Moreover, the achieved electrochemical performance of NaV_3O_8@10% PPy is also superior to those of previously reported NaV_3O_8 cathodes for NIBs. Based on the SEM images, it can be demonstrated that the excellent cycling stability of the NaV_3O_8@PPy composites is due to the unique core-shell structure that can protect the layered NaV_3O_8 nanosheets from splintering and enhance electrical conductivity of the composite, facilitating Na ion diffusion.

Acknowledgements

This work was financially supported by the National Natural Science Foundation of China (51231003), the Ministry of Education of China (IRT-13R30 and IRT-13022), and the 111 Project (B12015).

Notes and references

Institute of New Energy Material Chemistry, Collaborative Innovation Center of Chemical Science and Engineering (Tianjin), Key Laboratory of Advanced Energy Materials Chemistry (MOE), Tianjin Key Lab of Metal and Molecule-based Material Chemistry, Nankai University, Tianjin 300071, PR China, Tel.: +86 22 23504527; fax: +86 22 23504527; E-mail: jiaolf@nankai.edu.cn

1 S. Ong, V. Chevrier, G. Hautier, A. Jain, C. Moore, S. Kim, X. Ma and G. Ceder, *Energy Environ. Sci.*, 2011, **4**, 3680−3688.

2 Y-X. Wang, K. H. Seng, S-L. Chou, J-Z. Wang, Z-P. Guo, D.Wexler, H-K. Liu and S-X. Dou, *Chem. Commun.*, 2014, **50**, 10730-10733.

3 M. Winter, J. O. Besenhard, M. E. Spahr and P. Novak, *Adv. Mater.*,1998,**10**, 725-763.

4 D. Buchholz, A. Moretti, R. Kloepsch, S. Nowak, V. Siozios, M. Winter and S. Passerini, *Chem. Mater.*, 2013, **25**, 142−148.

5 V. Palomares, M. C. Cabanas, E. C. Martínez, M. H. Hanb and T. Rojo, *Energy Environ. Sci*., 2013, **6**, 2312−2337.

6 V. Palomares, P. Serras, I. Villaluenga, K. B. Hueso, J. C. Gonzalez and T. Rojo *Energy Environ. Sci.*, 2012, **5**, 5884-5901.

7 M. D. Slater, D. Kim, E. Lee and C. S. Johnson, *Adv. Funct. Mater.*, 2013, **23**, 947-958.

8 T-F. Zhou, W-K. Pang, C-F. Zhang, J-P. Yang, Z-X. Chen, H-K. Liu and Z-P. Guo, *ACS Nano*, 2014, **8**, 8323-8333.

9 Y-J. Zhu, Y-H. Xu, Y-H. Liu, C. L and C-S. Wang, *Nanoscale*, 2013, **5**, 780-787.

10 P. Barpanda, T. Ye, M. Avdeev, S. C. Chung and A. Yamada, *J. Mater. Chem. A*, 2013, **1**, 4194-4197.

11 P. Barpanda, J. Lu, T. Ye, M. Kajiyama, S. C. Chung, N. Yabuuchi, S. Komaba and A. Yamada, *RSC Adv.*, 2013, **3**, 3857–3860.

12 Y. U. Park, D. H. Seo, H. S. Kwon, B. Kim, J. Kim, H. Kim, I. Kim, H. I. Yoo and K. Kang, *J. Am. Chem. Soc.*, 2013, **135**, 13870−13878.

13 C. Zhu, K. Song, P. A. Aken, J. Maier Y. Yu, *Nano Lett.*, 2014, **14**, 2175−2180.

14 J. Liu, K. Tang, K-P. Song, P. A. V. Aken, Y. Yu and J. Maier, *Nanoscale*, 2014, **6**, 5081-5086.

15 C. Deng, S. Zhang and Y-X. Wu, *Nanoscale*, 2015, **7**, 487-491.

16 C-Z. Wu, Z-P. Hu, W. Wang, M. Zhang, J-L. Yang and Y. Xie, *Chem. Commun.*, 2008, 3891-3893.

17 N. A. Chernova, M. Roppolo, A. C. Dillon and M. S. Whittingham, *J. Mater. Chem.*, 2009, **19**, 2526–2552.

18 Y. Xue, X. D. Zhang, J. J. Zhang, J. Wu, Y. F. Sun, Y. C. Tian and Y. Xie, *J. Mater. Chem.*, 2012, **22**, 2560-2565.

19 H. Yu, X-H. Rui, H-T. Tan, J. Chen, X. Huang, C. Xu, W-L. Liu, Denis Y. W. Yu, H. H. Hng, H. E. Hosterb and Q-H. Y, *Nanoscale*, 2013, **5**, 4937-4943.

20 Y-N. Ko, Y-C. Kang and S. B. Park, *Nanoscale*, 2013, **5**, 8899 − 8903.

21 V. Raju, J. Rains, C. Gates, W. Luo, X-F. Wang, W. F. Stickle, G. D. Stucky and X-L. Ji, *Nano Lett.*, 2014, **14**, 4119−4124.

22 J. Cao, J. L. Musfeldt, S. Mazumdar, N. A. Chernova and M. S. Whittingham, *Nano. Lett.*, 2007, **7**, 2351-2355.

23 D-W. Su and G-X. Wang, *ACS Nano*, 2013, **7**, 11218-11226

24 H. M. Liu, H. S. Zhou, L. P. Chen, Z. F. Tang and W. S.Yang, *J. Power Sources*, 2011,**196**, 814 –819.

25 H. He, G. H. Jin, H. Y. Wang, X. B. Huang, Z. H. Chen, D. Sun and Y. G. Tang, *J. Mater. Chem. A*, 2014, **2**, 3563-3570.

26 D. Nguyen, J. Gim, V. Mathew, J. Song, S. Kim, D. Ahn, J. Kima, *ECS Electrochemistry Letters*, 2014, **3**, A69-A71.

27 M. E. Spahr, P. Novak, W. Scheifele, O. Haas and R. Nesper, *J. Electrochem. Soc.*, 1998, **145**, 421–427.

28 Y-H. Huang and J. B. Goodenough, *Chem. Mater.*, 2008, **20**, 7237-7241.

29 C-H. Xu, B-H. Xu, Y. Gu, Z-G. Xiong, J. Sun and X. S. Zhao, *Energy Environ. Sci.*, 2013, **6**, 1388-1414.

30 J. F. Zhao, S. C. Zhang, W. B. Liu, Z. J. Du and H. Fang, *Electrochim. Acta*, 2014, **121**, 428-433.

31 Z. G. Yin, Y. H. Ding, Q. D. Zheng and L. H. Guan, *Electrochem. Commun.*, 2012, **20**, 40-43.

32 Q. T. Qu, Y. S. Zhu, X. W. Gao. Y. P. Wu, *Adv. Energy Mater.*, 2012, **2**, 950-955.

33 W. Tang, L-L. Liu, S. Tian, Y-S. Zhu, Y-P. Wu, K. Zhu, *Energy Environ. Sci.*, 2012, **5**, 6909-6913.

34 Z. G. Yin and Q. D. Zheng, *Adv. Energy Mater.*, 2012, **2**, 179-218.

35 J. Zhang, Y. Yu, L. Liu and Y. Wu, *Nanoscale*, 2013, **5**, 3052 − 3057.

36 Y. Liu, B. H. Zhang, S. Y. Xiao, L. L. Liu, Z. B. Wen and Y. P. Wu, *Electrochim. Acta*, 2014, 116, 512-517.

37 J. Shao, X. Y. Li, L. Zhang, Q-T. Qu and H-H. Zheng, *Nanoscale*, 2013, **5**, 1460-1464.

38 H. Y. Wang, S. Q. Liu, Y. Ren, W. J. Wang and A. D.Tang, *Energy Environ. Sci.*, 2012, **5**, 6173-6179.

39 S. Q. Liang, J. Zhou, G. Z. Fang, J. Liu, Y. Tang, X. L. Li and A. Q. Pan, *ACS Appl. Mater. Interfaces*, 2013, **5**, 8704−8709.

40 M. Shirpour, J. Cabana and M. Doeff, *Energy Environ. Sci.*, 2013, **6**, 2538-2547.

41 G. Cho, B. M. Fung, D. T. Glatzhofer, J. S. Lee and Y. G. Shul, *Langmuir*, 2001, **17**, 456–461.

42 X. T. Zhang, J. Zhang, Z. F. Liu, C. Robinsonb, *Chem. Commun.*, 2004, 1852–1853.

43 B. Chen, J. Laverock, D. N. Jr., T. Y. Su, K. E. Smith, W. Wu, L. H. Doerrer, N. F. Quackenbush, S. Sallis, L. F. J. Piper, D. A. Fischer and J. C. Woicik, *J. Phys. Chem. C*, 2014, **118**, 1081−1094.

44 M. Demeter, M. Neumann and W. Reichelt, *Surf. Sci.*, 2000, **41**, 454–456.

45 H. He, X. G. Zeng, H. Y. Wang, N. Chen, D. Sun, Y. G. Tang, X. B. Huang and Y. F. Pan, *J. Electrochem. Soc*., 2015, 162, A39-A43.

46 J. Kawakita, M. Majima, T. Miura and T. Kishi, *J. Power Sources*, 1997, **66**, 135-139.

47 W. C. Duan, Z. Q. Zhu, H. Li, Z. Hu, K. Zhang, F. Y. Cheng, J. Chen, *J. Mater. Chem. A*, 2014, **2**, 8668-8675.